ADVANCED ELECTRONIC MATERIALS
www.advelectronicmat.de

Check for updates

n-Type Doping Effect of CVD-Grown Multilayer $MoSe_2$ Thin Film Transistors by Two-Step Functionalization

Seongin Hong, Haelin Im, Young Ki Hong, Na Liu, Sunkook Kim, and Jun Hong Park**

Molybdenum diselenide ($MoSe_2$) has attracted attention as a potential semiconductor platform. However, the as-synthesized $MoSe_2$ field-effect transistors (FETs) tend to exhibit the arbitrary properties of n-type, p-type, or ambipolar behavior due to the uncontrolled growth condition. Here, two-step functionalization is proposed to achieve n-doping effect and long-term stability in chemical vapor deposition (CVD)–grown $MoSe_2$ FETs using oxygen plasma treatment followed by the deposition of an Al_2O_3 layer. After the two-step surface functionalization procedure, three types of multilayer $MoSe_2$ FETs are all converted to n-type with the improvement of their electrical characteristics and stability; the n-doped multilayer $MoSe_2$ FETs exhibit an enhancement in field-effect mobility from 12.23 to 31.57 $cm^2\ V^{-1}\ s^{-1}$ and a 3 times higher I_{on}/I_{off}, compared to pristine multilayer $MoSe_2$ FETs. This enhancement of electric performance is attributed to the oxidation of topmost $MoSe_2$ to interfacial MoO_x with SeO_x induced by the oxygen plasma treatment, as well as to the existence of fixed positive charges in deposited Al_2O_3. The functionalized devices exhibit excellent stability against stress, as confirmed with negative bias illumination stress tests for 7200 s. Moreover, an environmental stability test for 21 days reveals no degradation in electric performance of $MoSe_2$ FETs.

2D layered transition metal dichalcogenides (TMDs) such as molybdenum disulfide (MoS_2), molybdenum diselenide ($MoSe_2$), tungsten disulfide (WS_2), and tungsten diselenide (WSe_2) have attracted intense interest as semiconductor platforms for next-generation electronic, optoelectronic, and flexible devices owing to their fascinating electrical, optical, and mechanical properties.[1–10] Moreover, TMDs have a finite bandgap resulted from the orbital overlap between the chalcogen atoms and transition metal atoms in the atomically thin body.[11–13] As a result, transistors based on TMDs are expected to show superior performances, which means that the application of TMDs can be broadened to digital logic,[14,15] memory,[16,17] or next-generation computation systems.[18,19] To fabricate complementary devices including n- and p-type field-effect transistors (FETs), an efficient doping process should be developed and, in addition, the long-term stability of these devices needs to be coupled.[20–25]

Owing to its superior photoactivity, $MoSe_2$ has recently been investigated for application in various fields, including energy storage, catalysis, and optoelectronic devices. Since the bandgap of $MoSe_2$ is smaller than that of MoS_2, a larger electrical conductivity can be expected in $MoSe_2$ FETs.[26–29] Additionally, it has been reported that since the Mo—Se bond is more stable than the Mo—S bond, the possibility of defect formation at the oxide–TMD channel interface is reduced, as a result of which, the noise current is lower in $MoSe_2$ than MoS_2.[30–32] However, during the synthesis process of $MoSe_2$ via chemical vapor transport (CVT) or chemical vapor deposition (CVD), uncontrolled defects states can be introduced in the $MoSe_2$ flakes, because of involving the high temperature and pressure environment to produce a single crystal mineral TMD. Therefore, the synthesized $MoSe_2$ FETs tend to randomly exhibit the characteristics of not only n-type behavior but also ambipolar or p-type behavior; as shown in previous results,[31,33–36] it has been reported that CVD- or CVT-grown $MoSe_2$ FETs can be ambipolar, n-dominant, or p-dominant transistors depending on the growth conditions. To enable the integration of CVD- or CVT-synthesized $MoSe_2$ in practical devices, these inhomogeneous characteristics of $MoSe_2$ FETs should be unipolar.

The present report demonstrates a process to achieve n-doping of CVD-grown multilayer $MoSe_2$ FETs via a two-step surface functionalization procedure that involves exposure to oxygen plasma followed by the deposition of an Al_2O_3 passivation layer using atomic layer deposition (ALD). The oxygen plasma treatment induces the formation of interfacial MoO_x layer at $MoSe_2$ and the reduction of hall current in all fabricated $MoSe_2$ FETs, while the on-current at n-branch is nearly constant. Moreover, thin MoO_x layer can provide nucleation sites with dangling bonds for the uniform deposition of ALD Al_2O_3. After the deposition of ALD Al_2O_3 on $MoO_x/MoSe_2$, I_{on}/I_{off} ratio of $MoSe_2$ FETs at n-branch is enhanced by up to 9.6 times

S. Hong, H. Im, Dr. Y. K. Hong, Dr. N. Liu, Prof. S. Kim
School of Advanced Materials Science & Engineering
Sungkyunkwan University
Suwon 440-745, Korea
E-mail: seonkuk@skku.edu

Prof. J. H. Park
School of Materials Science & Engineering
Gyeongsang National University
Jinju 52828, Korea
E-mail: yakte@gnu.ac.kr

Prof. J. H. Park
Department of Physics
Ewha Womans University
Seoul 03760, Republic of Korea

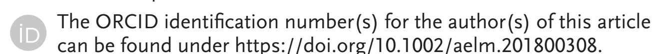
The ORCID identification number(s) for the author(s) of this article can be found under https://doi.org/10.1002/aelm.201800308.

DOI: 10.1002/aelm.201800308

© 2018 WILEY-VCH Verlag GmbH & Co. KGaA, Weinheim

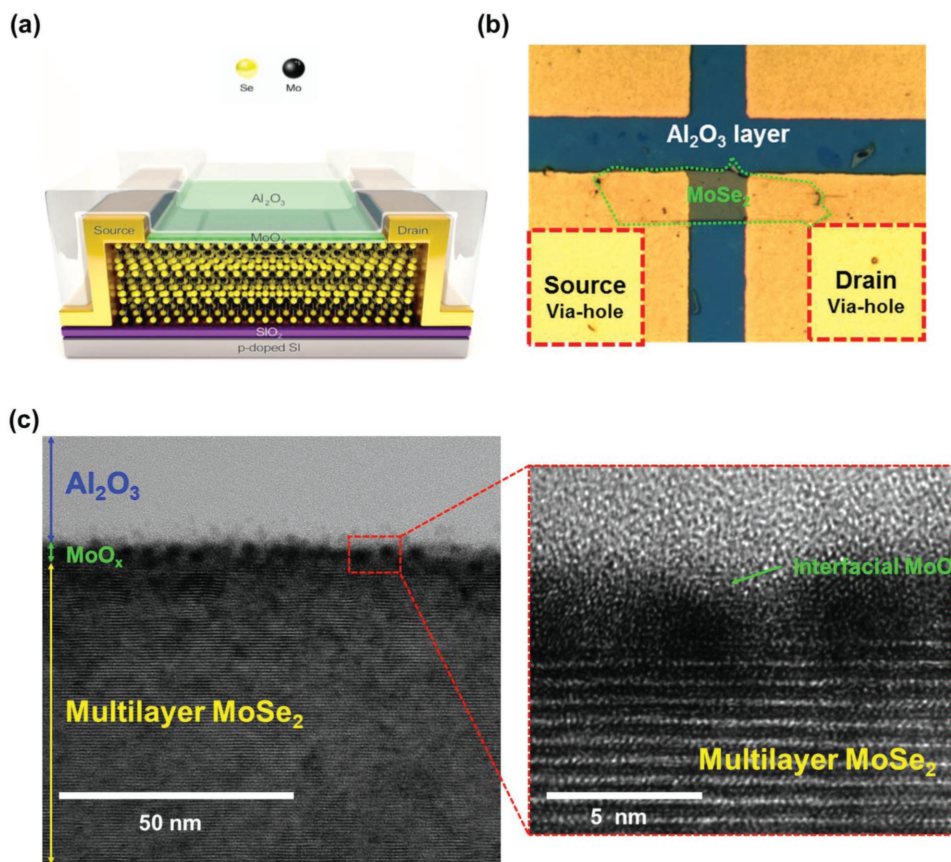

Figure 1. Two-step functionalized CVD-grown multilayer $MoSe_2$ thin film transistor. a) A schematic of the doping process using O_2 plasma treatment and Al_2O_3 passivation for the CVD-grown multilayer $MoSe_2$ FET. b) Optical microscopy image of a multilayer $MoSe_2$ FET after O_2 plasma and Al_2O_3 passivation. c) Cross-sectional TEM image of multilayer $MoSe_2$ after doping through O_2 plasma treatment and Al_2O_3 layer deposition. High-magnification cross-sectional TEM image of the top layer is shown in the right.

without compromising field-effect mobility and off-current, consistent with electrostatic doping. As a result, this two-step functionalization not only turns n-type $MoSe_2$ FETs into additionally enhanced n-type FETs but also transforms ambipolar and p-type $MoSe_2$ FETs into n-type FETs.

Figure 1a shows a schematic of the cross-section of the n-doped CVD-grown multilayer $MoSe_2$ FET prepared using the two-step process of oxygen plasma treatment and Al_2O_3 deposition. After the fabrication of $MoSe_2$ FETs, oxygen plasma treatment for 1 min followed by the deposition of a 40 nm thick Al_2O_3 layer was performed on the channel of the $MoSe_2$ device to achieve n-type doping and long-term stability. Figure 1b indicates the optical microscope image showing the top-view of the $MoSe_2$ FET after the two-step n-doping process. The thickness of the $MoSe_2$ flakes used in this study is about 50 nm to minimize the direct effect of SiO_2 substrate; it has been reported that the formation of interface of TMDs/SiO_2 can induce the charge trapping, resulting in extrinsic hysteresis or mobility degradation.[1,37,38] Therefore, to minimize the unintentional electric perturbation associated with the substrates, thick $MoSe_2$ channel is employed in the present report. Moreover, Das and Appenzeller[39] have reported the dependence of electrical property on the layer thickness of MoS_2 FETs; they mentioned that the field-effect mobility values strongly depend on the flake thickness in range from monolayer to few layers. Although the field-effect mobility of 50 nm $MoSe_2$ FETs in this report can be smaller than thinner $MoSe_2$ FETs (less than 30 nm), the 50 nm $MoSe_2$ FETs still show the reasonably moderate field-effect mobility to demonstrate the electric enhancement via the present two-step functionalization. Therefore, the performance of multilayer $MoSe_2$ transistors, presented in this paper, do not depend much on the layer number of $MoSe_2$ film. Transmission electron microscopy (TEM) was used to observe the interface of $MoSe_2$ after applying two-step functionalization consisting of oxygen plasma treatment and Al_2O_3 deposition, as shown in Figure 1c. The zoomed-in TEM image reveals that the oxygen plasma treatment induces the formation of new interfacial layer between the Al_2O_3 layer and the $MoSe_2$ multilayer.

To monitor the chemical transition of the CVD $MoSe_2$ multilayers following exposure to energetically activated O, X-ray photoelecton microscopy (XPS) was performed before and after applying O_2 plasma treatment. As shown in the black curve in **Figure 2**a, the XPS of bare $MoSe_2$ shows the chemical states of Mo 3d with two Mo peaks at 229.7 and 232.8 eV, assigned to Mo 3d5/2 and Mo 3d3/2, respectively.[40–42] However, after exposure of $MoSe_2$ to the O_2 plasma, a chemical change is induced, as shown by the red curve in Figure 2a, where the intensity of the Mo 3d5/2 peak at 229.7 eV decreases by ≈90%, while new peaks

© 2018 WILEY-VCH Verlag GmbH & Co. KGaA, Weinheim

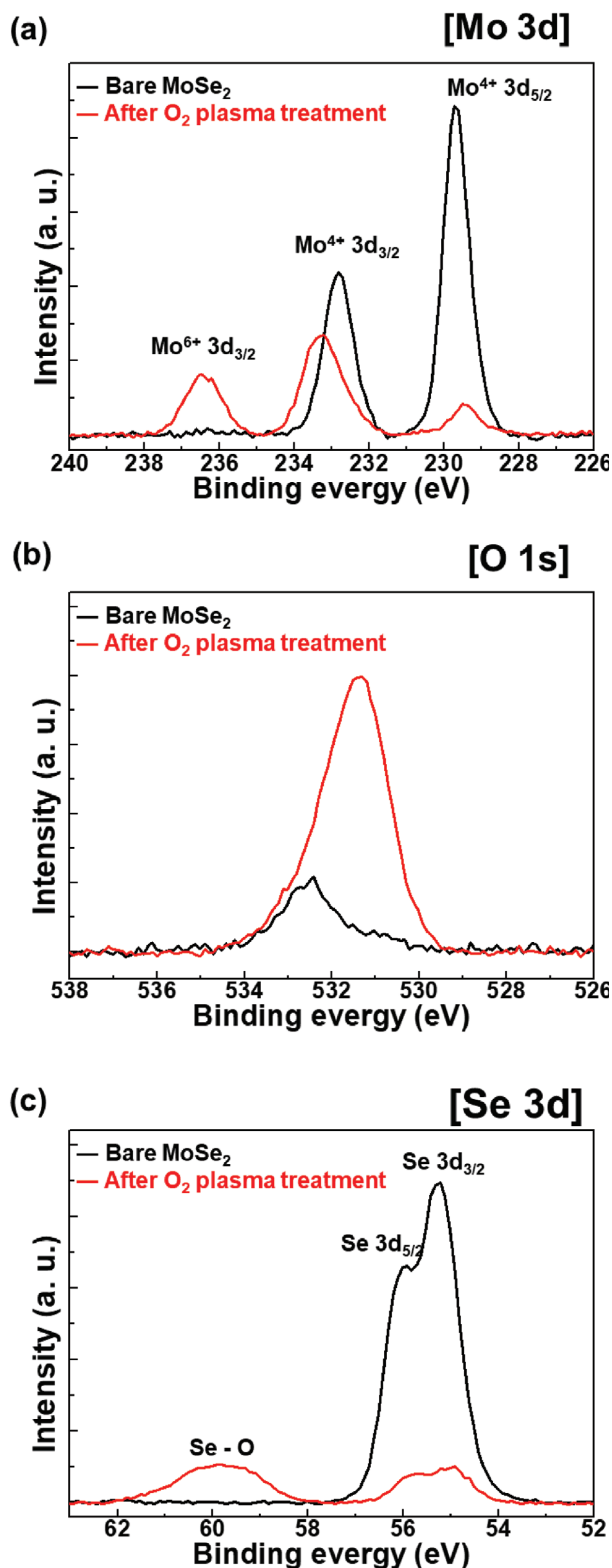

Figure 2. XPS surface analysis of atomic oxygen–doped multilayer $MoSe_2$. a) Mo 3d, b) Se 3d, and c) O 1s core levels measured from pristine $MoSe_2$ and after O_2 plasma treatment followed by annealing at 200 °C in an ALD chamber.

are observed at 233.3 and 236.5 eV, which is consistent with the formation of MoO_x.[43–45] The positions of the new Mo 3d peaks at higher binding energies compared to those in bare $MoSe_2$ indicates that the oxygen atoms attract additional electrons away from Mo atoms in the newly formed MoO_x.[43] It is noted that the peaks in $MoSe_2$ are broadened and have an asymmetric peak shape after the O_2 plasma treatment, consistent with the coexistence of multiple chemical compositions in the formed MoO_x. The oxidation of $MoSe_2$ via O_2 plasma treatment is also confirmed from the O 1s spectra of O_2 plasma–treated $MoSe_2$, as shown by the black curve in Figure 2b; a small signal of O 1s can be observed at 532.62 eV even before applying the O_2 plasma treatments. It is suggested that this O 1s signal results from the adsorption of oxygen-containing molecules introduced from ambient conditions on bare $MoSe_2$, or arises due to a partial oxidation of defects such as a step edge in the ambient conditions, after the CVD growth process.[46] In contrast, after applying the O_2 plasma treatment to $MoSe_2$, a strong O 1s signal appears at the binding energy of 531.3 eV, consistent with the formation of MoO_x.[44,45] Based on TEM image and XPS result, the thickness of MoO_x can be estimated to be about 3 nm, consistent with conversion of 3–5 $MoSe_2$ layers to MoO_x.

Similar chemical transitions can also be observed in the XPS spectra of Se 3d, as shown in Figure 2c; the XPS of bare $MoSe_2$ reveals a doublet at the binding energy ranged 55.3–56.0 eV, consistent with the two overlapped peaks of Se 3d3/2 and Se 3d5/2.[40,42] Contrastingly, after applying the O_2 plasma treatment, the intensity of the original Se peak decreases by ≈88%, while new peak corresponded to the formation of Se—O bonds appears at ≈60 eV.[47,48] Furthermore, the broad nature of this peak indicates that there are multiple binding configurations for the Se—O bonds. Thus, based on the XPS analysis, it is concluded that the top layer of $MoSe_2$ is partially oxidized to form MoO_x and SeO_x by the O_2 plasma treatment.

To investigate the influence of the n-doping process, the transfer characteristics of the three types $MoSe_2$ FETs showing n-type, ambipolar, and p-type behaviors were measured both before and after the two-step functionalization. **Figure 3**a shows the *I*–*V* transfer curves of CVD-grown multilayer $MoSe_2$ FET, which presents the transformation from typical n-type behavior (open dots) to additionally enhanced n-type (solid dots). After the doping process, the on-current increased from 6.0 to 15.1 µA and the threshold voltage (V_{th}) is shifted in the negative direction from −24.76 to −28.56 V, which are typical of n-doping.[49] On the other hand, the off-current remains in the tens of picoamperes range due to the combined effects of oxygen plasma treatment and Al_2O_3 deposition, which will be discussed in the following text. The field-effect electron mobility (μ_{FE}) and on/off current ratio (I_{on}/I_{off}) are improved by 2.58 and 3.34 times from 12.23 to 31.57 cm^2 V^{-1} s^{-1} and from 8.62×10^4 to 2.88×10^5, respectively. In addition, the presence of the Al_2O_3 layer reduces hysteresis by blocking the exposure to unintentional ambient molecules;[50,51] the effects of unintentional ambient molecules, such as O_2, H_2O, or carbon composites, on the channel of TMD FETs tend to degrade the performances of the device, including hysteresis.[50,52–56] Conversely, in present report, deposited Al_2O_3 dielectrics act as the passivation layers to effectively block the surface of the $MoSe_2$ from unintentional molecular adsorption, thereby only controlled

© 2018 WILEY-VCH Verlag GmbH & Co. KGaA, Weinheim

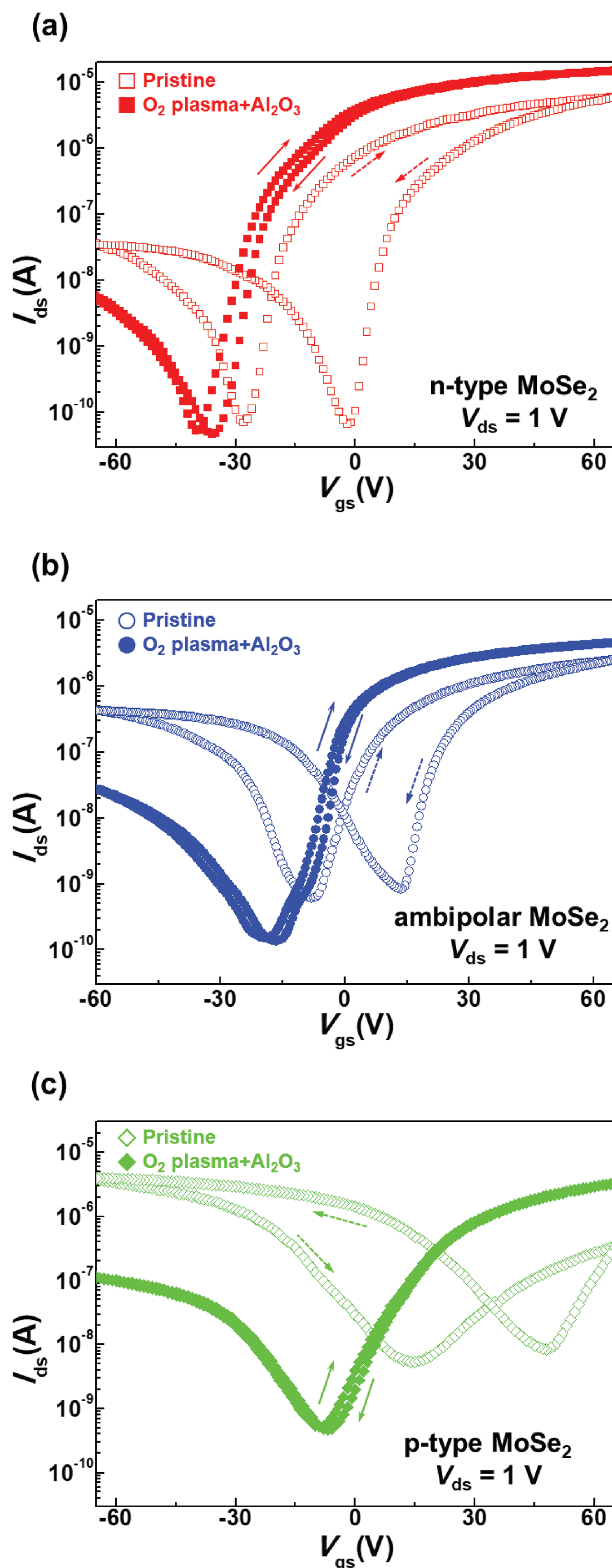

Figure 3. Electrical properties of atomic oxygen–doped multilayer $MoSe_2$ FETs. a) n-Type $MoSe_2$ FETs with 14.18 µm width (W) and 18.55 µm length (L). b) Ambipolar-type $MoSe_2$ FETs with 22.02 µm W and 25.42 µm L. c) p-Type $MoSe_2$ FETs with 21.69 µm W and 17.84 µm L. All fabricated $MoSe_2$ FETs are converted into the unipolar n-type $MoSe_2$ FETs, after the two-step functionalization. In present report, 50 nm $MoSe_2$ layers are employed as the channels in the FETs.

oxygen atoms can be intentionally introduced into $MoSe_2$ FETs to improve the electronic performance of $MoSe_2$ FETs. Similarly, both p-type and ambipolar $MoSe_2$ FETs with nearly symmetric electron and hole transport and p-type $MoSe_2$ FET are converted to n-type, as confirmed by the increased current at positive gate bias and decreased off-current at negative gate bias (Figure 3b,c). μ_{FE} of ambipolar and p-type $MoSe_2$ increased from 4.82 to 9.09 $cm^2\ V^{-1}\ s^{-1}$ and from 4.7 to 5.28 $cm^2\ V^{-1}\ s^{-1}$, respectively. These results indicate that our two-step process is a very promising technique for the n-type doping of CVD-grown multilayer $MoSe_2$ FETs with enhanced electrical characteristics and the ambipolar behavior of TMDs FETs can be converted to be unipolar. It is noted that the subthreshold slope of functionalized $MoSe_2$ FETs is also discussed in the Supporting Information.

The unipolar enhancement of $MoSe_2$ FET at n-branch is initiated by the current reduction at p-branch with O_2 plasma treatment. As shown in the electric characteristic of **Figure 4**a, although there is the sample to sample variation in the dominant doping behavior (n- or p-type), the most of bare multilayer $MoSe_2$ FETs have a large current at the both n- and p-branches resulting in degradation of off-current. However, after the O_2 plasma treatments, the current of all $MoSe_2$ FETs at p-branch decreases over an order of magnitude, while the current at n-branch is nearly constant. It has been known in previous reports that the various defects, such as vacancies or antisites in M—X—M structures, can be introduced during the CVD growth, resulting in existence of excess negative or positive charge carriers.[36,57,58] Moreover, the molecular adsorption of elementary Se, Mo, or ambient molecules on the surface of TMDs also can induce unintentionally electronic perturbation in TMDs.[59–61] Conversely, it can be hypothesized based on the present results that after applying O_2 plasma to $MoSe_2$ top layers, the density of positive charge carriers induced by defects decreases; during applying O_2 plasma, energetically activated atomic oxygen is exposed to layered $MoSe_2$, while top $MoSe_2$ layers is converted to nearly insulating ultrathin MoO_x layers. As a result, the atomic oxygen can be infiltrated or diffused into underneath $MoSe_2$ to form the covalent bonding with the defects sites of $MoSe_2$.[62–64] As defects states can be suppressed with the passivation of dangling bonds at defects of oxygen plasma treated $MoSe_2$, ambipolar $MoSe_2$ channel becomes unipolarly n-type $MoSe_2$ channel. It is noted that although the defects in underneath $MoSe_2$ can be passivated by atomic oxygen, the topmost of $MoSe_2$ can be damaged by the oxygen plasma, resulting in the formation of dangling bonds. However, this damage at the $MoO_x/MoSe_2$ surface can be passivated by followed deposition of Al_2O_3, which will be discussed below.

It is noted that the formation of MoO_x can improve the nucleation of ALD Al_2O_3 at the initial growth stage. Due to absence of dangling bonds at the basal plane of TMDs, the nucleation of ALD dielectric typically occurs at the only defects or step

© 2018 WILEY-VCH Verlag GmbH & Co. KGaA, Weinheim

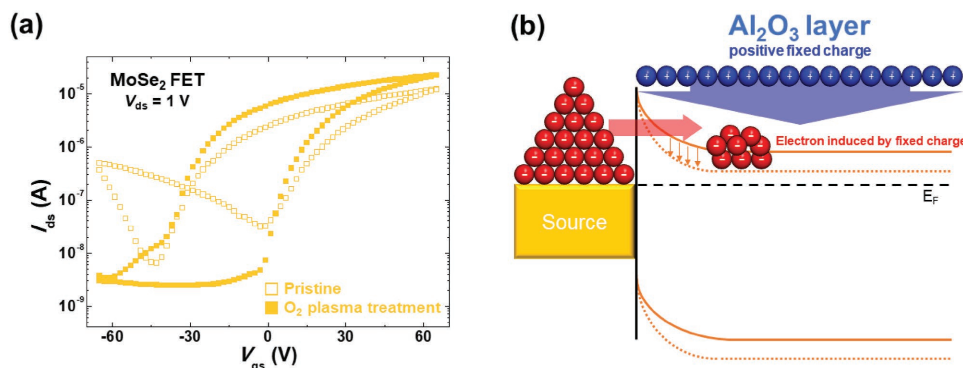

Figure 4. Mechanism of n-type doping effect though two-step functionalization. a) I_{ds}–V_{gs} curve of $MoSe_2$ FET before and after O_2 plasma treatment. b) Energy band diagram for metal (Ti/Au)–semiconductor ($MoSe_2$) junction.

edges, resulting in the existence of pinholes, consistent with the previous reports.[65,66] As a result, the inhomogeneous interface is formed between ALD dielectric and TMDs, thereby unintentional charge trapping or scattering can be induced during the operation of TMDs FETs.[67,68] Conversely, the formed MoO_x by O_2 plasma can act as interfacial layer between Al_2O_3 and $MoSe_2$ to improve the nucleation of Al_2O_3 with providing ALD reaction sites. It is noted that $MoO_x/MoSe_2$ FET without Al_2O_3 still shows nearly equivalent hysteresis to bare $MoSe_2$ FET; it can be hypothesized that existence of dangling bonds at $MoO_x/MoSe_2$ results in adsorption of large coverage of ambient molecules in ambient conditions. In addition, ≈3 nm thickness of MoO_x functional layer would not be enough to screen charge trapping induced by adsorption of ambient molecules at the surface of FETs.

Once unipolar n-dominant channels are obtained in $MoSe_2$ FETs by O_2 plasma treatment, the on-current (I_{on}) is additionally enhanced by the subsequent deposition of Al_2O_3 on $MoO_x/MoSe_2$. As shown in Figure 3a–c, the deposition of Al_2O_3 induces the increase of I_{on} at n-branch over an order of magnitude, consistent with n-doping. It is well known that as grown ALD high-*k* materials such as HfO_2 and Al_2O_3 typically is substoichiometric oxides, resulting in the existence of fixed charges[69–73] in ALD dielectric. Therefore, the fixed positive charges are uniformly distributed at the relatively thick Al_2O_3 overlayer (40 nm) on the O_2 plasma treated top surface of $MoSe_2$. Consequently, in the stack of $Al_2O_3/MoO_x/MoSe_2$, the negative carriers (electrons) are pulled to top layer of $MoSe_2$ by electrostatic force of positively charged Al_2O_3, and accumulated at the interface of functionalized $MoSe_2$, leading to the electrostatic n-type doping effect in the devices.[70–72] In the energy band diagram, it is seen that the width of Schottky barrier between Ti/Au electrodes and $MoSe_2$ is reduced due to the electron accumulation induced by the Al_2O_3 overlayer and thus, electron injection from the source to $MoSe_2$ is increased (Figure 4b); the positive fixed charge by Al_2O_3 can cause excess carriers (Δn) in the $MoSe_2$ channel, which results in the shift of the quasi-Fermi level (E_{Fn}) close to the conduction band (E_c). The created quasi-Fermi level for electrons results in the thinner Schottky barrier width, afterward, electrons can effectively inject through the thinning Schottky barrier, given by the equation

$$n = n_0 + \delta n = n_i \exp\frac{E_F - E_{Fi}}{kT} \quad (1)$$

where n_i and F_{Fi} are the intrinsic carrier concentration and intrinsic Fermi level, respectively. Therefore, thinning Schottky barrier width by Al_2O_3 on $MoSe_2$ FETs results in effective electrons injection, consistent with lowering the contact resistance. It is noted that the as-grown MoO_x is normally p-doped insulator similar with the ALD Al_2O_3, thereby electrostatic n-doping is not perturbated by MoO_x interfacial layers.

In addition, the reduction of the off-current in the $MoSe_2$ FETs fabricated in this study can be observed following the deposition of Al_2O_3 layers on O_2 plasma–treated $MoSe_2$ by ALD. As shown in Figure 3a–c, the transfer curves of all the $MoSe_2$ FETs reveal improvement in I_{on}/I_{off} following the deposition of ALD Al_2O_3. This result can be explained based on the observation that the electrically activated defects originated from the high temperatures process during CVD growth or high-energy damage during O_2 plasma treatments are passivated by the ALD Al_2O_3.[74] If the metal–chalcogen bonds are broken to form dangling bonds or defects at the TMD surface, additional shallow defect states can be formed (near the band edge) close to the bandgap or deep level defects (close to the Fermi level), depending on the defect configurations in the TMD.[57,58,75,76] Consequently, unintentional doping or poor I_{on}/I_{off} ratios in the TMD channels of the FET can result from the presence of metallic defect states, which can lead to excess charge carrier density and a reduction in bandgap.[77,78] In addition, during the O_2 plasma process, the direct exposure of the $MoSe_2$ surface to the O_2 plasma can, in addition to forming MoO_x layer via the oxidation of $MoSe_2$, leads to increased density of Se vacancies with nearly metallic dangling bonds on the topmost layer of $MoSe_2$. This can cause the off-current to be further degraded in $MoSe_2$ FETs.[77,79] It is noted that although these defects or dangling bonds formed at the surface of treated $MoSe_2$ can spontaneously react with extrinsic ambient molecules (such as hydrocarbon, O_2, or H_2O), the uncontrolled adsorption of molecules can induce substoichiometric oxidation or additional defective charge density in the channel.[80,81] However, the deposition of ALD Al_2O_3 at 473 K after O_2 plasma treatment can passivate all the metallic defects or dangling bonds by forming bonds with Al or O at the O_2 plasma–treated surface. Thus, the defect states in the O_2 plasma–treated $MoSe_2$ can be electrically deactivated to a certain level.[81–85] Therefore, it can be concluded that the I_{on}/I_{off} ratio of $MoSe_2$ FET can be improved by the two-step

© 2018 WILEY-VCH Verlag GmbH & Co. KGaA, Weinheim

O_2 plasma treatments and deposition of Al_2O_3 layer, which is consistent with the observed experimental results.

In summary, various defects states can be introduced in $MoSe_2$ during the CVD growth of $MoSe_2$ or the fabrication processes, thereby it can be hypothesized that these defects states induce the unintentional p-currents in $MoSe_2$ FETs. However, the density of positive charge carriers originated from the defects states near the top surface of $MoSe_2$ decreases with applying O_2 plasma to $MoSe_2$ FETs, consistent with the reduction of on-current at p-branch for all fabricated $MoSe_2$ FETs. After the reduction of p-branch current in $MoSe_2$ FETs with O_2 plasma, the deposition of Al_2O_3 layers induces electrostatic n-doping in $MoSe_2$ FETs, consistent with additional increase of on-current at n-branch of $MoSe_2$ FETs; the existence of uniformly distributed positive fixed charge in Al_2O_3 induces the formation of n-channel in $MoSe_2$ FETs with the accumulation of negative carriers near the interface of $Al_2O_3/MoO_x/MoSe_2$.

In order to evaluate the stability of the n-doped multilayer $MoSe_2$ FETs prepared in this work, we performed negative bias illumination stress (NBIS) and environmental stability tests. The NBIS test was performed on a multilayer $MoSe_2$ FET before and after doping under a light illumination of 1500 Nits with $V_{gs} = -30$ V and $V_{ds} = 1$ V for 7200 s, as shown in **Figure 5**a (undoped) and Figure 5b (doped). It is noted that all NBIS test was performed in ambient conditions, thereby ambient molecules can be introduced to the surface of fabricated $MoSe_2$ FETs. With increasing NBIS time, a negative shift in the V_{th} of the device before doping is clearly observed, contrast to the device after doping. Figure 5c also shows a comparison of the V_{th} shifts of multilayer $MoSe_2$ FET from 0 to 7200 s before and after doping, which are −6.91 and −0.58 V, respectively. Thus, the device stability is improved after doping. The shift in V_{th} under NBIS may be attributed to the adsorbed molecules on the top surface of $MoSe_2$ or due to the charge trapping of the photogenerated carriers at the $SiO_2/MoSe_2$ interface.[50,86] However, further research is needed to fully understand the mechanism of the negative shift in V_{th} of $MoSe_2$ FETs under a NBIS test. To test the environmental stability of the devices after doping, the transfer characteristics of doped $MoSe_2$ FETs were measured under ambient conditions for 21 days, as shown in Figure 5d. Our results show that the device exhibits superior doping stability, with no sign of degradation such as a shift in V_{th} and/or a reduced I_{on}/I_{off}.

In this study, the two-step n-doping process consisting of oxygen plasma treatment and deposition of an Al_2O_3 capping layer is proposed for CVD-grown multilayer $MoSe_2$ FETs with n-type, ambipolar, and p-type behaviors. Cross-sectional TEM and XPS surface analysis confirmed the presence of MoO_x interfacial layers formed by the oxygen plasma on the multilayer $MoSe_2$. The formation of the insulating Al_2O_3/MoO_x functionalization layer enhances the I_{on} at the n-branch with electrostatic n-doping of $MoSe_2$ channels. As a result, the randomly characterized as grown $MoSe_2$ with n-type, ambipolar, and p-type behaviors is transformed into the unipolar n-doped $MoSe_2$. Moreover, the improvement of electrical properties and the excellent doping stability were confirmed by comparing the electrical property behaviors of the pristine and doped $MoSe_2$ FETs; these results demonstrate the high efficacy of our doping process and highlight its great potential for application in future wearable electronics.

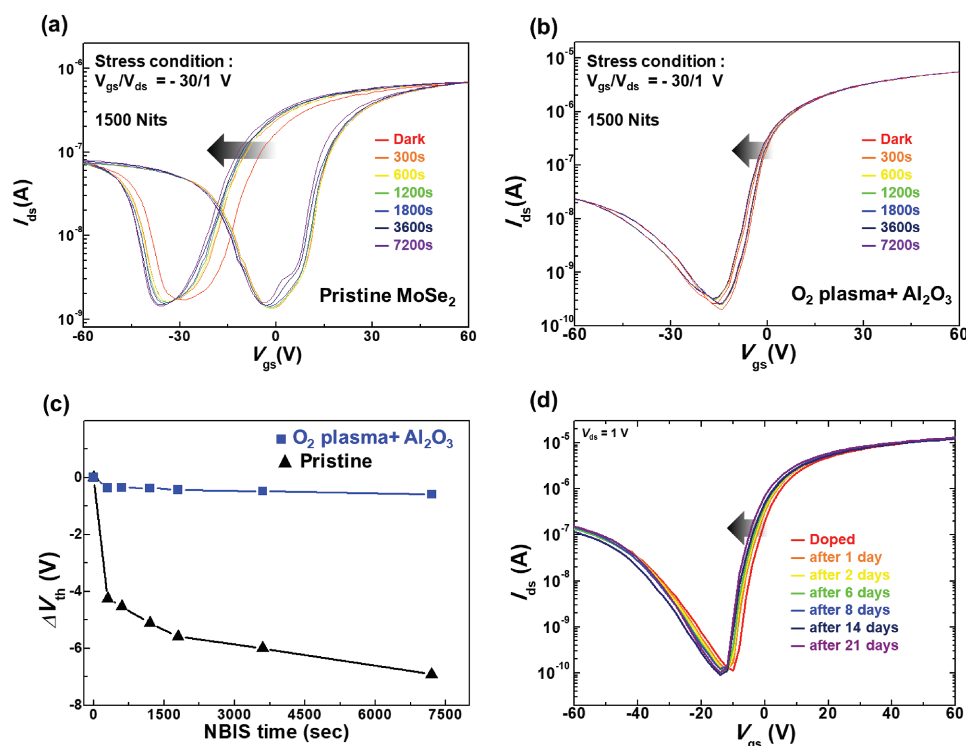

Figure 5. Stability test of atomic oxygen–doped multilayer $MoSe_2$ FETs. NBIS test results of a) pristine and b) doped multilayer $MoSe_2$ FETs. c) Comparisons of the shift in V_{th} derived from NBIS test results, d) environmental stability after three weeks in ambient air.

© 2018 WILEY-VCH Verlag GmbH & Co. KGaA, Weinheim

Experimental Section

Fabrication of CVD-Grown Multilayer $MoSe_2$ FETs: Bulk-like multilayer $MoSe_2$ was obtained by CVD under a relatively high pressure; the details of this process are reported in the previous work.[36] Mechanically exfoliated $MoSe_2$ flakes obtained from CVD-grown $MoSe_2$ by the conventional scotch tape method were transferred onto a heavily p-doped Si substrate that functioned as a back gate with a 300 nm thick SiO_2 layer as the gate insulator. Ti/Au (20/ 200 nm) source and drain electrodes were deposited by e-beam evaporation and patterned using standard photolithography techniques with wet etching. Finally, the as-fabricated devices were annealed in an Ar/H_2 atmosphere at 200 °C for 2 h to remove any organic residue and reduce the contact resistance between the electrodes and the $MoSe_2$ multilayer.

Two-Step Functionalization: The two-step functionalization process reported in this paper involves oxygen plasma treatment followed by Al_2O_3 passivation on $MoSe_2$ FETs. The oxygen plasma treatment was carried out using a reactive ion etching (RIE) system (NNS Vacuum, 17NNS01). During plasma treatment of the multilayer $MoSe_2$ FETs for 1 min, the pressure of the chamber, plasma power, and oxygen gas flow rate were maintained at 1×10^{-2} Pa, 100 W, and 30 standard cubic centimeters per minute (sccm), respectively. After oxygen plasma treatment, an Al_2O_3 layer was grown on the multilayer $MoSe_2$ FETs at 200 °C by ALD using NCD, Lucida 100. Trimethylaluminum (TMA) and water vapor (H_2O) were the sources of aluminum and oxygen, respectively. Each cycle (out of a total of 400 deposition cycles to obtain a 40 nm thick Al_2O_3 layer), consisted of TMA pulse (0.2 s), TMA purge (10 s), H_2O pulse (0.2 s), and H_2O purge (10 s). The thickness of source and drain in the $MoSe_2$ FETs were 220 nm (Ti/Au: 20/200 nm). Therefore, considering step coverage and total surface passivation of Al_2O_3 on $MoSe_2$ FETs, the thickness of Al_2O_3 was set to be relatively thick by 40 nm.

Measurement and Analysis Method: The electrical properties of pristine and n-doped CVD-grown multilayer $MoSe_2$ FETs were measured using a semiconductor parameter analyzer (Keithley 4200-SCS). NBIS test was performed at $V_{gs} = -30$ V and $V_{ds} = 1$ V from 0 to 7200 s with a light illumination of 1500 Nits using Keithley 4200-SCS and a halogen lamp (FOK-100W). The extent of oxygen penetration and the change in surface chemical composition in multilayer $MoSe_2$ FETs treated by oxygen plasma were determined by TEM (JEOL, JEM ARM 200F) and XPS (Thermo Electron, K-Alpha), respectively. The sample for cross-sectional TEM imaging was prepared by the focused-ion beam (FIB) technique using a JIB-4601F system from JEOL.LTD. The top view of the device after the two-step functionalization was observed by optical microscopy (BX51M, Olympus Co.). The field-effect mobilities (μ_{FE}) of the devices were calculated using the equation $\mu_{FE} = g_m(W/L)(C_iV_d)$, where g_m is the transconductance (dI_d/dV_g), W and L are, respectively, the channel width and length, C_i is the capacitance per unit area of the gate insulator, and V_d is the drain voltage.

Supporting Information

Supporting Information is available from the Wiley Online Library or from the author.

Acknowledgements

This research was supported in part by the National Research Foundation of Korea (Grant Nos. 2018R1A2B2003558, 2013M3C1A3059590, 2015R1A1A1A05027488). This work was supported by the Ministry of Trad, Industry and Energy (MOTIE) and the Korea Evaluation Industrial Technology (KEIT) through the Industrial Strategic Technology Development Program (Nos. 10079571 and 10080348).

Conflict of Interest

The authors declare no conflict of interest.

Keywords

Al_2O_3 passivation, molybdenum diselenide, n-type doping, O_2 plasma treatment, transition metal dichalcogenide

Received: May 13, 2018
Revised: August 14, 2018
Published online:

[1] S. Kim, A. Konar, W.-S. Hwang, J. H. Lee, J. Lee, J. Yang, C. Jung, H. Kim, J.-B. Yoo, J.-Y. Choi, *Nat. Commun.* **2012**, *3*, 1011.
[2] J. S. Rhyee, J. Kwon, P. Dak, J. H. Kim, S. M. Kim, J. Park, Y. K. Hong, W. G. Song, I. Omkaram, M. A. Alam, *Adv. Mater.* **2016**, *28*, 2316.
[3] Y. Zhang, Y. Zhang, Q. Ji, J. Ju, H. Yuan, J. Shi, T. Gao, D. Ma, M. Liu, Y. Chen, *ACS Nano* **2013**, *7*, 8963.
[4] H. Li, J. Wu, Z. Yin, H. Zhang, *Acc. Chem. Res.* **2014**, *47*, 1067.
[5] Q. H. Wang, K. Kalantar-Zadeh, A. Kis, J. N. Coleman, M. S. Strano, *Nat. Nanotechnol.* **2012**, *7*, 699.
[6] M. Chhowalla, H. S. Shin, G. Eda, L.-J. Li, K. P. Loh, H. Zhang, *Nat. Chem.* **2013**, *5*, 263.
[7] M. Xu, T. Liang, M. Shi, H. Chen, *Chem. Rev.* **2013**, *113*, 3766.
[8] A. K. Geim, I. V. Grigorieva, *Nature* **2013**, *499*, 419.
[9] X. Huang, Z. Zeng, H. Zhang, *Chem. Soc. Rev.* **2013**, *42*, 1934.
[10] D. Jariwala, V. K. Sangwan, L. J. Lauhon, T. J. Marks, M. C. Hersam, *ACS Nano* **2014**, *8*, 1102.
[11] Z. Lu, O. Lee, J. C. Wong, S. Salahuddin, *J. Mater. Res.* **2016**, *31*, 911.
[12] M. Rifliková, R. Martoňák, E. Tosatti, *Phys. Rev. B* **2014**, *90*, 035108.
[13] S. Bhattacharyya, A. K. Singh, *Phys. Rev. B* **2012**, *86*, 075454.
[14] M. Tosun, S. Chuang, H. Fang, A. B. Sachid, M. Hettick, Y. Lin, Y. Zeng, A. Javey, *ACS Nano* **2014**, *8*, 4948.
[15] T. Roy, M. Tosun, X. Cao, H. Fang, D.-H. Lien, P. Zhao, Y.-Z. Chen, Y.-L. Chueh, J. Guo, A. Javey, *ACS Nano* **2015**, *9*, 2071.
[16] C. Ko, Y. Lee, Y. Chen, J. Suh, D. Fu, A. Suslu, S. Lee, J. D. Clarkson, H. S. Choe, S. Tongay, *Adv. Mater.* **2016**, *28*, 2923.
[17] W. Li, J. Li, *Nat. Commun.* **2016**, *7*, 10843.
[18] V. K. Sangwan, H.-S. Lee, H. Bergeron, I. Balla, M. E. Beck, K.-S. Chen, M. C. Hersam, *Nature* **2018**, *554*, 500.
[19] D. Sarkar, X. Xie, W. Liu, W. Cao, J. Kang, Y. Gong, S. Kraemer, P. M. Ajayan, K. Banerjee, *Nature* **2015**, *526*, 91.
[20] S. Das, M. Dubey, A. Roelofs, *Appl. Phys. Lett.* **2014**, *105*, 083511.
[21] D.-H. Kang, J. Shim, S. K. Jang, J. Jeon, M. H. Jeon, G. Y. Yeom, W.-S. Jung, Y. H. Jang, S. Lee, J.-H. Park, *ACS Nano* **2015**, *9*, 1099.
[22] H.-Y. Park, M.-H. Lim, J. Jeon, G. Yoo, D.-H. Kang, S. K. Jang, M. H. Jeon, Y. Lee, J. H. Cho, G. Y. Yeom, *ACS Nano* **2015**, *9*, 2368.
[23] D. Kiriya, M. Tosun, P. Zhao, J. S. Kang, A. Javey, *J. Am. Chem. Soc.* **2014**, *136*, 7853.
[24] P. Zhao, D. Kiriya, A. Azcatl, C. Zhang, M. Tosun, Y.-S. Liu, M. Hettick, J. S. Kang, S. McDonnell, S. KC, *ACS Nano* **2014**, *8*, 10808.
[25] S. Hong, G. Yoo, D. H. Kim, W. G. Song, O. K. Le, Y. K. Hong, K. Takahashi, I. Omkaram, D. N. Son, S. Kim, *Phys. Status Solidi C* **2017**, *14*, 1600262.
[26] S. Kim, J. Maassen, J. Lee, S. M. Kim, G. Han, J. Kwon, S. Hong, J. Park, N. Liu, Y. C. Park, *Adv. Mater.* **2018**, *30*, 1705542.
[27] A. Eftekhari, *Appl. Mater. Today* **2017**, *8*, 1.
[28] C.-P. Yang, Y.-X. Yin, Y.-G. Guo, *J. Phys. Chem. Lett.* **2015**, *6*, 256.

© 2018 WILEY-VCH Verlag GmbH & Co. KGaA, Weinheim

[29] S. Mao, Z. Wen, S. Ci, X. Guo, K. K. Ostrikov, J. Chen, *Small* **2015**, *11*, 414.
[30] X. Xie, D. Sarkar, W. Liu, J. Kang, O. Marinov, M. J. Deen, K. Banerjee, *ACS Nano* **2014**, *8*, 5633.
[31] S. R. Das, J. Kwon, A. Prakash, C. J. Delker, S. Das, D. B. Janes, *Appl. Phys. Lett.* **2015**, *106*, 083507.
[32] Y.-H. Chang, W. Zhang, Y. Zhu, Y. Han, J. Pu, J.-K. Chang, W.-T. Hsu, J.-K. Huang, C.-L. Hsu, M.-H. Chiu, *ACS Nano* **2014**, *8*, 8582.
[33] D. N. Ortiz, I. Ramos, N. J. Pinto, M.-Q. Zhao, V. Kumar, A. C. Johnson, *AIP Adv.* **2018**, *8*, 035014.
[34] N. R. Pradhan, D. Rhodes, Y. Xin, S. Memaran, L. Bhaskaran, M. Siddiq, S. Hill, P. M. Ajayan, L. Balicas, *ACS Nano* **2014**, *8*, 7923.
[35] B. Chamlagain, Q. Li, N. J. Ghimire, H.-J. Chuang, M. M. Perera, H. Tu, Y. Xu, M. Pan, D. Xaio, J. Yan, *ACS Nano* **2014**, *8*, 5079.
[36] C. Jung, S. M. Kim, H. Moon, G. Han, J. Kwon, Y. K. Hong, I. Omkaram, Y. Yoon, S. Kim, J. Park, *Sci. Rep.* **2015**, *5*, 15313.
[37] R. Decker, Y. Wang, V. W. Brar, W. Regan, H.-Z. Tsai, Q. Wu, W. Gannett, A. Zettl, M. F. Crommie, *Nano Lett.* **2011**, *11*, 2291.
[38] W. Bao, X. Cai, D. Kim, K. Sridhara, M. S. Fuhrer, *Appl. Phys. Lett.* **2013**, *102*, 042104.
[39] S. Das, J. Appenzeller, *Phys. Status Solidi RRL* **2013**, *7*, 268.
[40] M.-W. Chen, D. Ovchinnikov, S. Lazar, M. Pizzochero, M. B. Whitwick, A. Surrente, M. Baranowski, O. L. Sanchez, P. Gillet, P. Plochocka, *ACS Nano* **2017**, *11*, 6355.
[41] X. Wang, Y. Gong, G. Shi, W. L. Chow, K. Keyshar, G. Ye, R. Vajtai, J. Lou, Z. Liu, E. Ringe, *ACS Nano* **2014**, *8*, 5125.
[42] A. Wa'el A, A. Nelson, *J. Mater. Sci.* **2005**, *40*, 2679.
[43] A. T. Martín-Luengo, H. Köstenbauer, J. Winkler, A. Bonanni, *AIP Adv.* **2017**, *7*, 015034.
[44] T. H. Chiang, H. C. Yeh, *Materials* **2013**, *6*, 4609.
[45] K. Kanai, K. Koizumi, S. Ouchi, Y. Tsukamoto, K. Sakanoue, Y. Ouchi, K. Seki, *Org. Electron.* **2010**, *11*, 188.
[46] S. Vishwanath, X. Liu, S. Rouvimov, P. C. Mende, A. Azcatl, S. McDonnell, R. M. Wallace, R. M. Feenstra, J. K. Furdyna, D. Jena, *2D Mater.* **2015**, *2*, 024007.
[47] Y. Fan, Y. Zhuo, L. Li, *Appl. Surf. Sci.* **2017**, *420*, 465.
[48] D. Rajamanickam, P. Dhatshanamurthi, M. Shanthi, *Spectrochim. Acta, Part A* **2015**, *138*, 489.
[49] M. Iqbal, O. Kelekci, M. Iqbal, J. Eom, *Carbon* **2013**, *59*, 366.
[50] N. Liu, J. Baek, S. M. Kim, S. Hong, Y. K. Hong, Y. S. Kim, H.-S. Kim, S. Kim, J. Park, *ACS Appl. Mater. Interfaces* **2017**, *9*, 42943.
[51] S. H. Jeong, N. Liu, H. Park, Y. K. Hong, S. Kim, *Appl. Sci.* **2018**, *8*, 424.
[52] A. J. Arnold, A. Razavieh, J. R. Nasr, D. S. Schulman, C. M. Eichfeld, S. Das, *ACS Nano* **2017**, *11*, 3110.
[53] T. Li, G. Du, B. Zhang, Z. Zeng, *Appl. Phys. Lett.* **2014**, *105*, 093107.
[54] D. J. Late, B. Liu, H. R. Matte, V. P. Dravid, C. Rao, *ACS Nano* **2012**, *6*, 5635.
[55] H. Qiu, L. Pan, Z. Yao, J. Li, Y. Shi, X. Wang, *Appl. Phys. Lett.* **2012**, *100*, 123104.
[56] S. Davis, J. Carver, *Appl. Surf. Sci.* **1984**, *20*, 193.
[57] M. Pandey, F. A. Rasmussen, K. Kuhar, T. Olsen, K. W. Jacobsen, K. S. Thygesen, *Nano Lett.* **2016**, *16*, 2234.
[58] S. Zhang, C.-G. Wang, M.-Y. Li, D. Huang, L.-J. Li, W. Ji, S. Wu, *Phys. Rev. Lett.* **2017**, *119*, 046101.
[59] S. H. Chae, Y. Jin, T. S. Kim, D. S. Chung, H. Na, H. Nam, H. Kim, D. J. Perello, H. Y. Jeong, T. H. Ly, *ACS Nano* **2016**, *10*, 1309.
[60] X. Li, Y. Fang, S. Wu, Z. Zhu, *AIP Adv.* **2015**, *5*, 057143.
[61] J. Chang, S. Larentis, E. Tutuc, L. F. Register, S. K. Banerjee, *Appl. Phys. Lett.* **2014**, *104*, 141603.
[62] A. Azcatl, X. Qin, A. Prakash, C. Zhang, L. Cheng, Q. Wang, N. Lu, M. J. Kim, J. Kim, K. Cho, *Nano Lett.* **2016**, *16*, 5437.
[63] A. Nipane, D. Karmakar, N. Kaushik, S. Karande, S. Lodha, *ACS Nano* **2016**, *10*, 2128.
[64] J. Lu, A. Carvalho, X. K. Chan, H. Liu, B. Liu, E. S. Tok, K. P. Loh, A. Castro Neto, C. H. Sow, *Nano Lett.* **2015**, *15*, 3524.
[65] J. H. Park, S. Fathipour, I. Kwak, K. Sardashti, C. F. Ahles, S. F. Wolf, M. Edmonds, S. Vishwanath, H. G. Xing, S. K. Fullerton-Shirey, *ACS Nano* **2016**, *10*, 6888.
[66] A. Azcatl, K. Santosh, X. Peng, N. Lu, S. McDonnell, X. Qin, F. De Dios, R. Addou, J. Kim, M. J. Kim, *2D Mater.* **2015**, *2*, 014004.
[67] C. M. Jackson, A. R. Arehart, E. Cinkilic, B. McSkimming, J. S. Speck, S. A. Ringel, *J. Appl. Phys.* **2013**, *113*, 204505.
[68] A.-J. Cho, S. Yang, K. Park, S. D. Namgung, H. Kim, J.-Y. Kwon, *ECS Solid State Lett.* **2014**, *3*, Q67.
[69] P. Peacock, J. Robertson, *Appl. Phys. Lett.* **2003**, *83*, 2025.
[70] J. Na, M.-K. Joo, M. Shin, J. Huh, J.-S. Kim, M. Piao, J.-E. Jin, H.-K. Jang, H. J. Choi, J. H. Shim, *Nanoscale* **2014**, *6*, 433.
[71] T. Li, B. Wan, G. Du, B. Zhang, Z. Zeng, *AIP Adv.* **2015**, *5*, 057102.
[72] H. Lee, J. H. Kim, C. J. Lee, *Appl. Phys. Lett.* **2016**, *109*, 222105.
[73] H. A. Lee, S. Y. Kim, J. Kim, W. Choi, *J. Phys. D: Appl. Phys.* **2017**, *50*, 094001.
[74] Z. Lin, B. R. Carvalho, E. Kahn, R. Lv, R. Rao, H. Terrones, M. A. Pimenta, M. Terrones, *2D Mater.* **2016**, *3*, 022002.
[75] D. Liu, Y. Guo, L. Fang, J. Robertson, *Appl. Phys. Lett.* **2013**, *103*, 183113.
[76] J. H. Park, A. Sanne, Y. Guo, M. Amani, K. Zhang, H. C. Movva, J. A. Robinson, A. Javey, J. Robertson, S. K. Banerjee, *Sci. Adv.* **2017**, *3*, e1701661.
[77] Z. Yu, Y. Pan, Y. Shen, Z. Wang, Z.-Y. Ong, T. Xu, R. Xin, L. Pan, B. Wang, L. Sun, *Nat. Commun.* **2014**, *5*, 5290.
[78] K. Santosh, R. C. Longo, R. Addou, R. M. Wallace, K. Cho, *Nanotechnology* **2014**, *25*, 375703.
[79] Z. Wu, Z. Luo, Y. Shen, W. Zhao, W. Wang, H. Nan, X. Guo, L. Sun, X. Wang, Y. You, *Nano Res.* **2016**, *9*, 3622.
[80] R. Addou, C. M. Smyth, J.-Y. Noh, Y.-C. Lin, Y. Pan, S. M. Eichfeld, S. Fölsch, J. A. Robinson, K. Cho, R. M. Feenstra, *2D Mater.* **2018**, *5*, 025017.
[81] C. J. Flynn, S. M. McCullough, E. Oh, L. Li, C. C. Mercado, B. H. Farnum, W. Li, C. L. Donley, W. You, A. J. Nozik, *ACS Appl. Mater. Interfaces* **2016**, *8*, 4754.
[82] A. u. Rehman, M. F. Khan, M. A. Shehzad, S. Hussain, M. F. Bhopal, S. H. Lee, J. Eom, Y. Seo, J. Jung, S. H. Lee, *ACS Appl. Mater. Interfaces* **2016**, *8*, 29383.
[83] H.-V. Han, A.-Y. Lu, L.-S. Lu, J.-K. Huang, H. Li, C.-L. Hsu, Y.-C. Lin, M.-H. Chiu, K. Suenaga, C.-W. Chu, *ACS Nano* **2016**, *10*, 1454.
[84] H. Nan, Z. Wang, W. Wang, Z. Liang, Y. Lu, Q. Chen, D. He, P. Tan, F. Miao, X. Wang, *ACS Nano* **2014**, *8*, 5738.
[85] J. Schmidt, B. Veith, R. Brendel, *Phys. Status Solidi RRL* **2009**, *3*, 287.
[86] J. Kim, B. Seo, S. Lee, S. Jeong, Y. Roh, *J. Nanosci. Nanotechnol.* **2017**, *17*, 7327.

© 2018 WILEY-VCH Verlag GmbH & Co. KGaA, Weinheim